



CoMn-S/CDs nanocomposite for effective long wavelength visible-light-driven photocatalytic water splitting

Yijun Fu, Cheng Zhu, Changan Liu, Mengling Zhang, Huibo Wang, Weilong Shi, Hui Huang*, Yang Liu*, Zhenhui Kang*

Jiangsu Key Laboratory for Carbon-Based Functional Materials & Devices, Institute of Functional Nano & Soft Materials (FUNSOM), Soochow University, 199 Ren'ai Road, Suzhou, 215123, Jiangsu, PR China



ARTICLE INFO

Keywords:

Transition metal sulfide
Photocatalyst
CoMn-S/CDs
Water splitting
Long wavelength visible light driven

ABSTRACT

Photocatalytic water splitting to produce hydrogen is one of the important ways to solve energy crisis. Most transition metal sulfide semiconductors which have wide optical band gap are impractical for long wavelength visible light driven water splitting. Therefore, modulation of broad band gap has become a significant strategy and a huge challenge to achieve efficient catalyst for photocatalytic water splitting. Here, we report the synthesis of a ternary photocatalyst MnS/CoS₂/CDs applied for long wavelength visible-light-driven water splitting without the requirement for any sacrificial agents. The optimal MnS/CoS₂/CDs nanocomposite (CoMn-S/CDs) as an effective photocatalyst exhibits excellent photocatalytic activity with H₂ evolution rate of 0.421 μmol/h and O₂ evolution rate of about 0.051 μmol/h under visible light irradiation (420 nm ≤ λ ≤ 700 nm) when the concentration of CDs is 0.039 g_{CDs}/g_{catalyst}. In particular, the H₂ evolution rate is 0.076 μmol/h and O₂ evolution rate is about 0.010 μmol/h at λ = 535 nm while the H₂ evolution rate is 0.024 μmol/h and O₂ evolution rate is about 0.004 μmol/h at λ = 630 nm. The efficient photocatalytic activity may attribute to the synergistic effect of the ternary structures, in which MnS is the major component for photocatalysis, addition of CoS₂ component enables the photocatalyst to capture light of wider range and CDs provide reduction sites.

1. Introduction

Photocatalytic water splitting is one of the most promising strategies for converting solar energy into clean and carbon-neutral hydrogen fuels [1,2]. In recent years, semiconductor photocatalysts such as transition metal sulfides have been widely studied [1–3]. However, many transition metal sulfides with broad band gap cannot be used to catalyse water splitting for their poor visible light utilization efficiency and high recombination percentage of photogenerated electron-hole pairs [4,5]. MnS is such a candidate with appropriate energy band that can reduce H⁺ to H₂ and oxidize H₂O to O₂ in theory. MnS has attracted considerable interest because of its magnetic and magneto-optical properties [6]. However, the photocatalytic activity of MnS is limited to that the irradiation light is located on the UV region due to the broad band gap of 3.00 eV, hence it can only be excited by photons with wavelengths below 413 nm [7]. In addition, it has been researched that the ultraviolet light accounted for only 5% in the solar spectrum while visible light accounted for about 43%. This limits the efficient utilization of solar energy by MnS. Besides, some other problems also remain to be solved for the applications of MnS, such as the fast recombination

of photogenerated electron-hole pairs, photo-corrosion and require for additional sacrificial agents in the photocatalytic system. Ikeue reported that the addition of a small amount of Cd to form Mn-Cd-S with band gap of 2.40 eV realized visible-light-driven hydrogen evolution [8]. Yuan reported that Janus-like MnS/Cu₇S₄ realized Z-scheme photocatalytic water splitting under broadband light irradiation [9]. However, the above two systems still need the help of sacrificial agents to realize the hydrogen production which is still not sustainable enough from economic perspective. Thus, modulation of band gap by combination is the key to realizing transition metal sulfides for solar photocatalytic decomposition of water and photocatalytic water splitting without sacrificial agents also needs further exploration.

Transition metal dichalcogenide compounds with pyrite structure, such as CoS₂, show various magnetic, electronic and optical properties [10]. CoS₂ is semiconductor material with narrow band gap and high sunlight utilization efficiency [11]. It has been confirmed to be efficient in the degradation of pollutants and photocatalytic hydrogen production [12]. Carbon quantum dots (CDs), as one kind of new carbon nanomaterials with diameters less than 10 nm [13], possess many special physical and chemical properties. CDs have attracted more and more

* Corresponding authors.

E-mail addresses: hhuang0618@suda.edu.cn (H. Huang), yangl@suda.edu.cn (Y. Liu), zhkang@suda.edu.cn (Z. Kang).

attention due to advantages of functional surface moieties, unique electron reservoir, photo-induced electron transfer property, stability, and high specific surface area [14–16]. Recently, CDs have been reported in some very important work as significant components or co-catalysts in photocatalytic solar water splitting systems [17].

Here, we report the design and fabrication of a new kind of photocatalyst CoMn-S/CDs by combining MnS with CDs and CoS₂, in which the band gap of CoMn-S/CDs could be estimated to achieve long wavelength visible-light-driven water splitting. By controlling the amount of CDs, the CoMn-S/CDs exhibits excellent water splitting property with H₂ evolution rate of 0.421 μmol/h and O₂ evolution rate of about 0.051 μmol/h (420 nm ≤ λ ≤ 700 nm), when the concentration of CDs is 0.039 g_{CDs}/g_{catalyst}. In particular, the H₂ evolution rate is 0.076 μmol/h and O₂ evolution rate is about 0.010 μmol/h when λ = 535 nm while the H₂ evolution rate is 0.024 μmol/h and O₂ evolution rate is about 0.004 μmol/h when λ = 630 nm. It is also notable that CoMn-S/CDs exhibits well stability for about 4-time repetitive experiments, which is better than many other transition metal sulfide catalysts [4]. The efficient photocatalytic ability may attribute to the synergistic effect of nanocomposite, in which MnS is the major component for photocatalysis, addition of CoS₂ component enables the photocatalyst to capture light of wider range and CDs serve as reduction sites, which not only accelerate the electron transfer to avoid recombination of photo induced electron-hole pairs but also simultaneously accept electrons to produce hydrogen.

2. Experimental section

2.1. Instrument and materials

The reagents are all purchased from Sigma and Alfa Aesar without further purification. Transmission electron microscopy (TEM), high-resolution transmission electron microscopy (HRTEM) was measured by using a FEI-Tecnai F20 transmission electron microscope with an accelerating voltage of 200 kV. The scanning electron microscope (SEM) and energy dispersive spectrometer (EDS) function were both applied to characterize the surface morphology and element contents of the samples. Powder X-ray diffraction (XRD) was carried out to characterize the crystal structure of the as-prepared products by using a PIXcel3D X-ray diffractometer (Empyrean, Holland Panalytical) with Cu K α radiation ($\lambda = 0.154178$ nm). The fourier transform infrared (FTIR) spectrum of the samples was acquired from a Hyperion spectrophotometer (Bruker) at the scan range of 400–4000 cm⁻¹. Raman spectra were collected by using a HR 800 Raman spectroscope (J Y, France) with a 20 mW air-cooled argon ion laser (633 nm) as the excitation source. UV/VIS/NIR spectrophotometer (Lambda 750, PerkinElmer) was employed to acquire the UV-vis absorption spectra. A Horiba Jobin Yvon (Fluoro Max-4) luminescence spectrometer was employed to record the photoluminescence (PL) spectra. X-ray photo-electron spectroscopy (XPS) measurements were conducted on a KRATOS Axis ultra-DLD X-ray photo-electron spectrometer with a monochromatic Mg K α X-ray source ($h\nu = 1283.30$ eV). Ultraviolet photo-electron spectroscopy (UPS) measurements were performed with He I (21.22 eV) as the monochromatic light source and a total instrumental energy resolution of 100 MeV.

2.2. Synthesis of CDs

CDs were obtained by an electrolytic method [16], with two graphite rods (from Alfa Aesar Co. Ltd.) as carbon sources. First, we cleaned the graphite rods in deionized water with ultrasonic agitation. Then cleaned rods were inserted into ultrapure water (18.5 MΩ cm⁻¹, 1000 mL) as cathode and anode. A bias of 30 V was applied between the two electrodes using a direct current power supply. The electrolysis process was running for 10 days under magnetic stirring until the colorless solution turned dark. After that, we filtered the dark solution

with a slow-speed quantitative filter paper to remove the precipitated graphite oxide and big graphite particles. Finally, we obtained CDs powder by freeze drying the filtered solution.

2.3. Synthesis of CoMn-S nanocomposite

The Co(NO₃)₂·6H₂O (1.164 g), C₄H₆MnO₄·4H₂O (1.94 g), NH₄F (0.36 g) and urea (1.2 g) were dissolved in deionized water (80 mL) in a 250 mL breaker. Then the solution was transferred to a 100 mL Teflon-lined stainless steel autoclave after vigorous stirring for a few minutes. The autoclave was sealed and heated at 120 °C for 6 h in oven and then cooled down to room temperature naturally. The hydrothermal product was collected by centrifugation. Then the product was washed by ethanol and distilled water respectively for several times. The hydrothermal product was placed in the hot center of a horizontal tube furnace after mixing with sulfur powder (1 g) in a porcelain boat. The samples were heated at 450 °C for 2 h in N₂ atmosphere. After that, the CoMn-S nanocomposite was obtained.

2.4. Synthesis of CoMn-S/CDs nanocomposite

The Co(NO₃)₂·6H₂O (1.164 g), C₄H₆MnO₄·4H₂O (1.94 g), NH₄F (0.36 g), urea (1.2 g) and CDs (0.02 g) were dissolved in deionized water (80 mL) in a 250 mL breaker. Then the solution was transferred to a 100 mL Teflon-lined stainless steel autoclave after vigorous stirring for a few minutes. The autoclave was sealed and heated at 120 °C for 6 h in oven and then cooled down to room temperature naturally. The hydrothermal product was collected by centrifugation. Then the product was washed by ethanol and distilled water respectively for several times. The hydrothermal product was placed in the hot center of a horizontal tube furnace after mixing with sulfur powder (1 g) in a porcelain boat. The samples were heated at 450 °C for 2 h in N₂ atmosphere. The CoMn-S/CDs nanocomposite was obtained.

2.5. Photocatalytic activity evaluation

Photocatalytic reactions were carried out in a multichannel photochemical reaction system (PCX50A Discover, Beijing Perfectlight Co. Ltd, China), and a bandpass filter was used to get visible light (420 nm ≤ λ ≤ 700 nm, λ = 535 nm and λ = 630 nm). Approximately 0.1 g of the photocatalysts were dispersed by a magnetic stirrer in 15 mL ultrapure water. The suspension is thoroughly bubbled with N₂ to remove air and irradiated in the photochemical reaction system for 20 h. To detect the gas production, a gas chromatograph (GC-7900) set up with a 5 Å molecular sieves column and a thermal conductivity detector (TCD) was utilized. N₂ was used as the carrier gas.

3. Results and discussion

Fig. 1a shows the SEM image of CoMn-S/CDs. The product typically has a sphere-like morphology with the diameter of 3 μm. Compared with SEM image of CoMn-S (Fig. S1a), the incorporation of CDs makes no change to the morphology of sphere. Fig. 1b and c displays the TEM images of CoMn-S/CDs, indicating that CDs (yellow circles) are uniformly dispersed on the surface of CoMn-S. The high-resolution TEM (HRTEM) image is presented in Fig. 1d, in which shows well-resolved lattice fringes with interplanar distances of 0.21 nm, 0.26 nm and 0.32 nm indexed to (100) [18], (200) [19] and (111) [20] planes of CDs, MnS and CoS₂, respectively. HRTEM image of CoMn-S is shown in Fig. S1b, which also shows the lattice fringes of 0.26 nm and 0.32 nm are corresponding to (200) [19] and (111) [20] planes of MnS and CoS₂, respectively. HAADF-STEM image and corresponding elemental mapping images of CoMn-S/CDs are shown in Fig. 1e–k, illustrating that the CoMn-S/CDs sample consisted of Co, Mn, S, C elements are evenly distributed. Similarly, Fig. S1c–h shows Co, Mn, and S elements are evenly distributed in the CoMn-S sample.

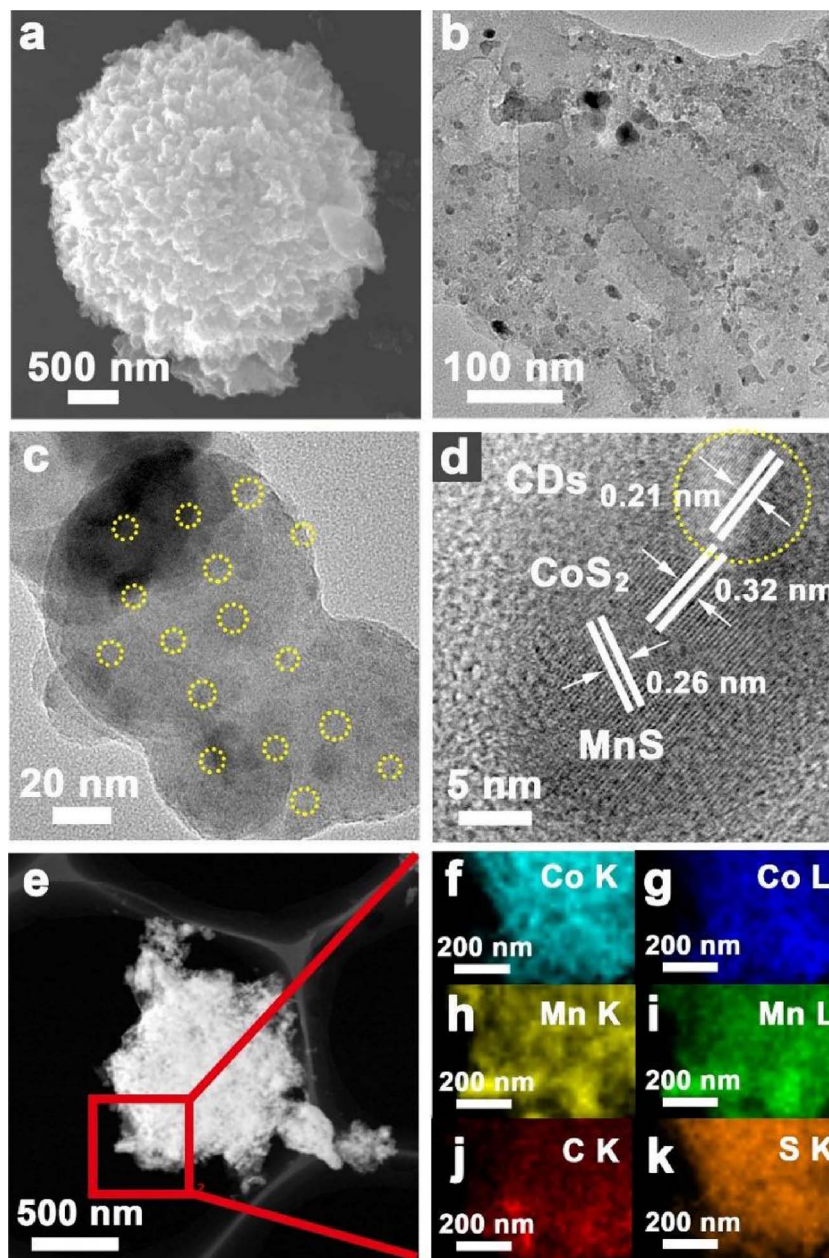


Fig. 1. (a) SEM images of CoMn-S/CDs ($0.039 \text{ g}_{\text{CDs}}/\text{g}_{\text{catalyst}}$). (b) TEM images of CoMn-S/CDs. (c) The magnified TEM image of CoMn-S/CDs with monodispersed CDs (yellow circles) on CoMn-S. (d) HRTEM image of CoMn-S/CDs. (e) HAADF-STEM image and (f-k) corresponding elemental mapping images of CoMn-S/CDs. (For interpretation of the references to colour in this figure legend, the reader is referred to the web version of this article.)

Fig. 2a shows the XRD patterns of CoMn-S/CDs (red line), MnS (blue line) and CoS_2 (black line). The XRD pattern of CoMn-S/CDs reveals the high crystallinity and the diffraction peaks are well indexed to CoS_2 (JCPDS No. 41-1471) and MnS (JCPDS No. 65-891) [19]. Nevertheless, no characteristic peak for carbon at 26° can be detected for the amount of CDs in CoMn-S/CDs was relatively low. XRD pattern of CoMn-S is shown in Fig. S2. Fig. S3 shows that after the photocatalytic reaction, the components of catalyst remain unchanged. The functional groups of CDs (black trace) and CoMn-S/CDs (red trace) measured by FTIR spectroscopy are provided in Fig. 2b, where they both show prominent peaks located at 3436, 1632, 1385 and 1100 cm^{-1} , which can be assigned to the stretching vibrations of OH, C=O, C–O and C–O–C derived from CDs, respectively [21,22]. It is obvious that the Raman spectra of both CDs and CoMn-S/CDs show two prominent peaks centered at around 1325 and 1584 cm^{-1} , which are ascribed to the D band of the presence of sp^3 defects, and G band due to in-plane vibration of sp^2 carbon [23]. In contrast, the Raman spectrum of CoMn-S is shown in Fig. S4, where there are no recognizable peaks. All the data above have verified the combination of two transition metal sulfides and CDs.

Photoluminescence (PL) spectra of CoMn-S/CDs (red line) and CoMn-S (black line) with an excitation wavelength of 350 nm are presented in Fig. 2d, exhibiting that there is no distinctly change of peak positions with the incorporation of CDs except for the intensity. CoMn-S/CDs exhibits a weaker emission in the range of 400 – 600 nm than that of CoMn-S, indicating that the photo-generated charge carriers were transferred from CoMn-S to CDs in CoMn-S/CDs nanocomposites [24]. Fig. S5 shows N_2 adsorption-desorption isotherms and pore size distribution curves for CoMn-S/CDs. The Brunauer–Emmett–Teller (BET) specific surface area of CoMn-S/CDs was calculated to $6.5336 \text{ m}^2/\text{g}$.

Fig. 3 displays XPS spectra of CoMn-S/CDs with CDs concentration of $0.039 \text{ g}_{\text{CDs}}/\text{g}_{\text{catalyst}}$. XPS full spectrum of CoMn-S/CDs is offered in Fig. S6, showing peaks of elements Co, Mn, C, O and S. Peaks of C and O originate from the CDs. The core level Co 2p spectrum is shown in Fig. 3a, where two peaks at binding energy of 778.2 eV and 780.4 eV are corresponding to $\text{Co } 2p_{3/2}$, another two peaks at binding energy of 794.0 eV and 797.2 eV are corresponding to $\text{Co } 2p_{1/2}$ [25–27], indicating that the valence of cobalt is $+2$ [18]. The two relatively weak peaks at 785.5 eV and 802.7 eV belong to the shakeup satellites

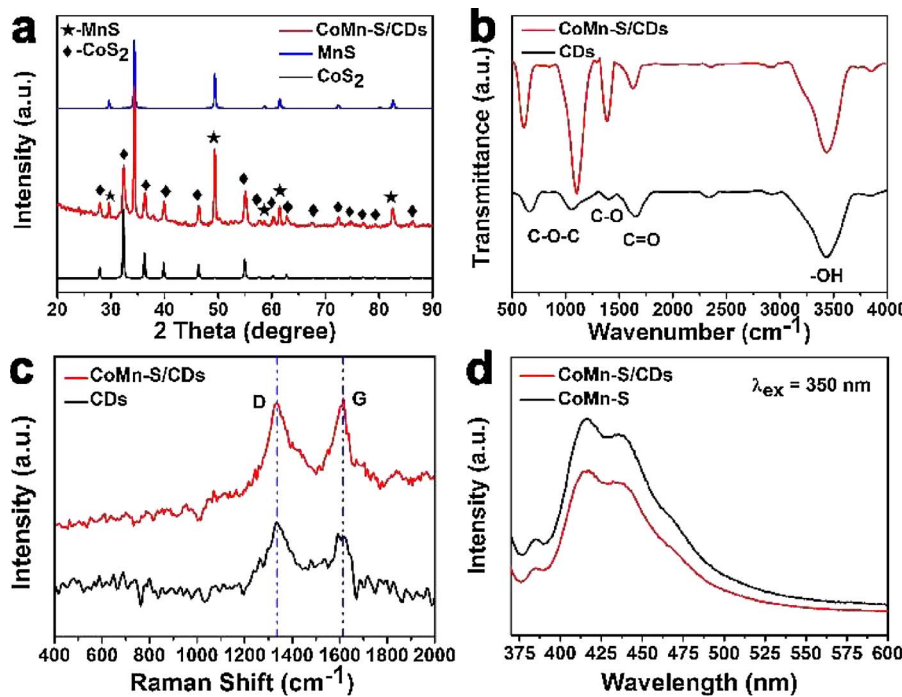


Fig. 2. (a) XRD patterns of CoMn-S/CDs (red line), MnS (blue line) and CoS₂ (black line). (b) FTIR spectra of CoMn-S/CDs (red line) and CDs (black line). (c) Raman spectra of CoMn-S/CDs (red line) and CDs (black line). (d) PL spectra of CoMn-S/CDs (red line) and CoMn-S (black line) with excitation wavelength of 350 nm (For interpretation of the references to colour in this figure legend, the reader is referred to the web version of this article.)

[25,26]. Fig. 3b shows the high-resolution XPS spectrum of Mn 2p with two peaks at 642.1 eV and 653.9 eV which correspond to Mn 2p_{3/2} and Mn 2p_{1/2}, respectively, hence is associated with Mn²⁺ [28,29]. The relatively weak peaks at binding energy of 645.5 eV and 657.5 eV are shakeup satellites [30]. Fig. 3c describes high-resolution XPS the spectrum of S 2p, in which the peak at binding energy of 161.7 eV in S 2p_{3/2} region corresponds to S²⁻, while peak at binding energy of 163.1 eV comes from S₂²⁻ and S–C bond [28,31,32], demonstrating the existence of Co–S–C or Mn–S–C bond. The binding energy at 168.2 eV is considered to be high oxidation state of S [12]. The high-resolution C 1s XPS spectrum (Fig. 3d) is deemed to be the atomic states of CDs loaded on CoMn-S, where the peak at 284.8 eV is assigned

to the C–C of the graphite structure of CDs, meanwhile the binding energy at 285.3, 286.2 and 288.3 eV can be attributed to the C–S, C–O and C=O bond, respectively [21,32–34]. The existence of C–S bond further validates the existence of Co–S–C or Mn–S–C bond. High-resolution XPS spectra of CoMn–S for Co 2p, Mn 2p and S 2p are shown in Fig. S7, indicating there is no change compared with CoMn-S/CDs.

Derived from the UV-vis absorption spectrum of CoMn-S/CDs (Fig. S8a), the optical band gap of CoMn-S/CDs can be estimated from the Tauc plot [8,35]. The curve of converted $(\alpha h\nu)^2$ versus $(h\nu)$ from the UV-vis spectrum is presented in Fig. S8b, in which α , h , and ν are the absorption coefficient, Planck constant, and light frequency, respectively, with $r = 2$ for a direct band gap material and $r = 1/2$ for an

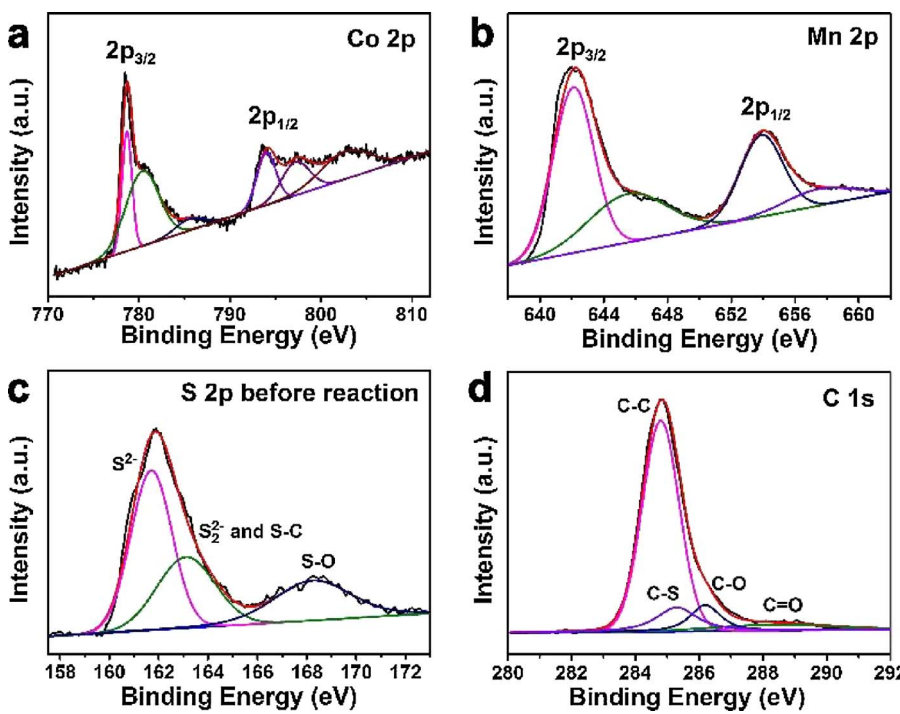


Fig. 3. High-resolution XPS spectra of CoMn-S/CDs for (a) Co 2p, (b) Mn 2p, (c) S 2p and (d) C 1s. All the CoMn-S/CDs have the same concentration of CDs with 0.039 g_{CDs}/g_{catalyst}.

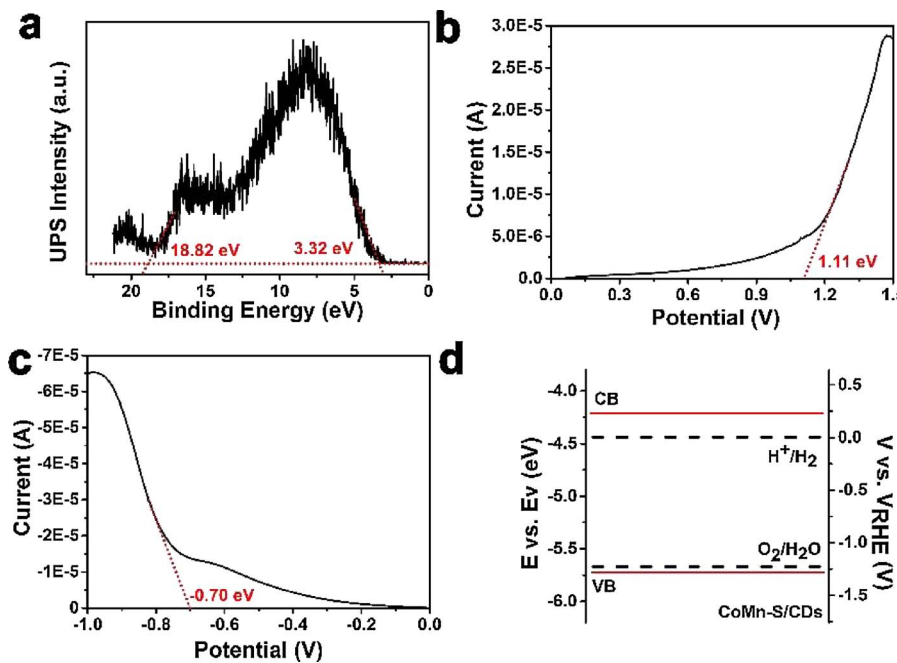


Fig. 4. (a) UPS spectrum of CoMn-S/CDs. The horizontal dotted line red lines mark the baseline and the tangents of the curve, where the intersections of the tangents and the baseline show the edges of the UPS spectrum, hence determining the UPS width. (b) Oxidation linear sweep voltammogram of CoMn-S/CDs on a modified glassy carbon electrode in acetonitrile + 0.1 M TBAPF₆ with 10 mV/s at room temperature. (c) Reduction linear sweep voltammogram of CoMn-S/CDs on the same modified glassy carbon electrode in acetonitrile + 0.1 M TBAPF₆ with 10 mV/s at room temperature. (d) Band structure diagram for CoMn-S/CDs. The CDs concentration in above samples is 0.039 g_{CDs}/g_{catalyst}. (For interpretation of the references to colour in this figure legend, the reader is referred to the web version of this article.)

indirect band gap material [14]. According to the previous study, CoMn-S is a direct band gap material [36]. As displayed in Fig. S8b, the two intersections of the tangent lines and the baseline denote the band gap energies. Thus, the band gap of CoMn-S/CDs is estimated to be 1.60 eV. Furthermore, ultraviolet photo-electron spectroscopy (UPS) was used to determine conduction band and valence band levels of a photocatalyst with reference to the redox potentials of the reaction. From the UPS spectrum, the ionization potential (equivalent to the valence band energy (E_v) of CoMn-S/CDs was calculated to be 5.72 eV by subtracting the width of the He I UPS spectra (Fig. 4a) from the excitation energy (21.22 eV). The conduction band energy E_c was thus estimated at 4.12 eV from E_v - E_g. The E_g, E_v, and E_c values of CoMn-S/CDs in electron volts are converted to electrochemical energy potentials in volts according to the reference standard for which 0 V versus RHE (reversible hydrogen electrode) equals -4.44 eV versus vac (vacuum level). Fig. 4b and c show the oxidation and reduction linear sweep

voltammogram of monodisperse CoMn-S/CDs nanocomposite modified on a glassy carbon electrode in acetonitrile + 0.1 M TBAPF₆ at 10 mV/s at room temperature, respectively. The quasi-reversible oxidation and reduction waves were recorded at 1.11 V and -0.70 V. The HOMO and LUMO levels were estimated to about -5.81 eV and -4.00 eV [37–40]. The optical band gap was calculated about 1.81 eV, which is close to the calculated band gap from ultraviolet photoelectron spectroscopy and UV-vis absorption spectrum. Therefore, the addition of CoS₂ component could enable the photocatalyst to capture light of wider range. Fig. 4d further shows that the conduction band of CoMn-S/CDs is above the reduction level for H₂O to H₂ and the valence band is below the oxidation level for H₂O to O₂. Band gap characterizations of CoMn-S are shown in Fig. S8c, d, S9 and S10, indicating there is no difference of band gap between CoMn-S and CoMn-S/CDs. Therefore, the CDs didn't change the band gap of CoMn-S.

Fig. 5a presents the dependence of gases evolution (H₂ and O₂)

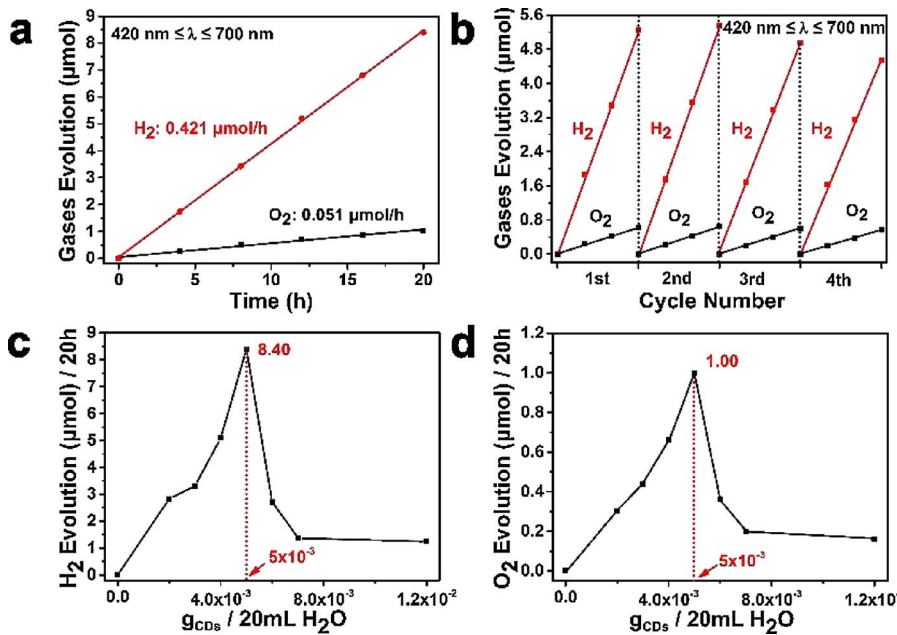


Fig. 5. (a) Dependence of H₂/O₂ evolution from water on time course under visible light irradiation (420 nm ≤ λ ≤ 700 nm) by CoMn-S/CDs (0.039 g_{CDs}/g_{catalyst}) as photocatalyst. (b) The cyclic stability of CoMn-S/CDs (0.039 g_{CDs}/g_{catalyst}) for photocatalytic water splitting under visible light. Comparisons of H₂ evolution (c) and O₂ evolution (d) in 20 h over CoMn-S/CDs with different concentration of CDs in 20 mL H₂O.

from water on time course under visible light irradiation ($420 \text{ nm} \leq \lambda \leq 700 \text{ nm}$) catalysed by CoMn-S/CDs (0.039 g_{CDs}/g_{catalyst}), indicating CoMn-S/CDs exhibits excellent hydrogen evolution property (0.421 $\mu\text{mol}/\text{h}$) when the concentration of CDs is 0.039 g_{CDs}/g_{catalyst}. The O₂ production (0.051 $\mu\text{mol}/\text{h}$) is very low compared to H₂, which is not equal to the mole ratio of 1:2 (O₂:H₂), demonstrating that the photo-corrosion is partly restrained when introducing CDs into CoMn-S. To determine the stability of CoMn-S/CDs, the cyclic stability experiments were carried out (Fig. 5b), which exhibited favourable stability for a catalyst dried and reused for 4 times (for each time is 12 h visible light irradiation ($420 \text{ nm} \leq \lambda \leq 700 \text{ nm}$)). Fig. 5c and d depicts the comparisons of H₂ and O₂ evolutions reacting for 20 h over 0.1 g CoMn-S/CDs with different CDs concentrations of CDs in 20 mL H₂O, respectively, which demonstrate that when the CDs concentration is 0.039 g_{CDs}/g_{catalyst}, the photocatalysts result in the optimal H₂ production (8.40 μmol) and O₂ production (1.00 μmol) in the same time course compared with other concentrations. Note that when the concentration of CDs is 0 (CoMn-S), there was neither hydrogen nor oxygen evolution (Fig. S11).

Based on the results above, it is explicit that the introduction of CoS₂ has changed the band gap of MnS and CDs endow the composite photocatalytic properties under visible light irradiation. In order to assess the long wavelength utilization efficiency of the as-prepared photocatalyst, photocatalytic water splitting was carried out under several given wavelengths. Similarly, as shown in Fig. 6, the H₂ evolution rate is 0.076 $\mu\text{mol}/\text{h}$ and O₂ evolution rate is about 0.010 $\mu\text{mol}/\text{h}$ when $\lambda = 535 \text{ nm}$ while the H₂ evolution rate is 0.024 $\mu\text{mol}/\text{h}$ and O₂ evolution rate is about 0.004 $\mu\text{mol}/\text{h}$ when $\lambda = 630 \text{ nm}$. It also exhibits fine stability for about 4-time repetitive experiments. Fig. S12 shows transient photocurrent response of CoMn-S/CDs under (a) visible light irradiation ($\lambda > 420 \text{ nm}$) and (b) different specific wavelengths. And they show photocurrent response both under visible light irradiation ($\lambda > 420 \text{ nm}$) and long specific wavelengths [41,42].

Based on the above experiments, we found both MnS and CoMn-S cannot catalyse water splitting under visible light, which may attribute to the wide band gap and high recombination percentage of photo-generated electron-hole pairs. Addition of CoS₂ component enables the photocatalyst to capture light of wider range but does not solve the problem of electron-hole recombination. Also, we found both MnS/CDs and CoS₂/CDs cannot catalyse water splitting under visible light, for that addition of CDs cannot modulate the band gap of CoMn-S. The

CoMn-S/CDs exhibits excellent photocatalytic activity for long wavelength visible-light-driven water spilling ($420 \text{ nm} \leq \lambda \leq 700 \text{ nm}$, $\lambda = 535 \text{ nm}$ and $\lambda = 630 \text{ nm}$), which could be attributed to several reasons that CDs can accelerate the electron transfer to avoid recombination of photo induced electron-hole pairs and accept electrons to produce hydrogen, further restrain the photo-corrosion of CoMn-S and stabilize the catalyst in a period. Luminescence decays (455 nm excitation, 550 nm emission) of CDs are shown in Fig. S13a and b, which were quenched by the known electron acceptor 2,4-dinitrotoluene (−0.9 V vs. NHE) and electron donor N,N-diethylaniline (DEA, 0.88 V vs. NHE), with the observed Stern-Volmer (insets of Fig. S13a and b) quenching constants ($K_{SV} \tau_F^0 k_q$) from linear regression of 10.52 M^{-1} and 5.80 M^{-1} , respectively [43]. The above results that CDs were quenched by either electron acceptors or electron donors, are clearly confirming that CDs are excellent as both electron acceptors and electron donors. Therefore, electrons will transfer from conduction band of CoMn-S to the surface of CDs and H⁺ will be reduced to H₂. Holes in the valence band of CoMn-S will oxidize H₂O to O₂ and react with S^{2−} to form high oxidation state of S (such as S₂O₃^{2−}), corroding catalysts gradually and leading the non-stoichiometry ratio of H₂ and O₂. Fig. 7a, b and S14a–c present XPS spectra of S2p before and after photocatalytic reaction, where the new peaks at the binding energy of 164.33 eV and 167.00 eV belong to elemental sulphide and S₂O₃^{2−}, respectively [44,45], demonstrating that after the reaction, high oxidation state of S has formed. However, Fig. 7c, d and S14d–i show that after the photocatalytic reaction, Co 2p and Mn 2p make no obvious change.

Fig. 8a–c show HRTEM images of reduction site of CoMn-S/CDs. The red and blue circles represent Ag and CDs particles, respectively. In the experiment, AgNO₃ was employed as indicator to clarify the reduction site in CoMn-S/CDs. As shown in Fig. 8e, Ag particles were deposited on the surface of CDs. Clear lattice spacing of 0.21 nm and 0.23 nm are in good agreement with the (100) plane of CDs and (111) lattice planes of Ag [17], respectively. It turned out that CDs are playing the role of active sites for hydrogen evolution.

Briefly, with broad band gap of 3.00 eV and high recombination percentage of photogenerated electron-hole pairs, MnS cannot produce hydrogen with the light radiation above 413 nm and without the help of sacrificial agent. Addition of CoS₂ component enables the photocatalyst to capture light of wider range. When incorporation with CDs, CDs can serve as reduction sites, which can accelerate the electron transfer to

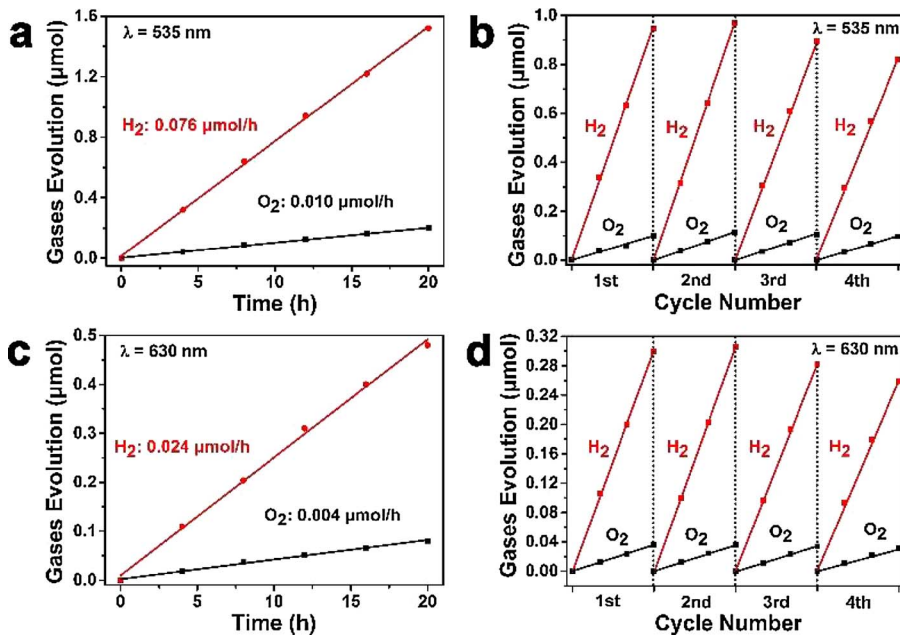


Fig. 6. Dependence of H₂/O₂ evolution from water on time course under visible light irradiation ((a) $\lambda = 535 \text{ nm}$, (c) $\lambda = 630 \text{ nm}$) by CoMn-S/CDs (0.039 g_{CDs}/g_{catalyst}) as photocatalyst. The cyclic stability of CoMn-S/CDs (0.039 g_{CDs}/g_{catalyst}) for photocatalytic water splitting under visible light ((b) $\lambda = 535 \text{ nm}$, (d) $\lambda = 630 \text{ nm}$).

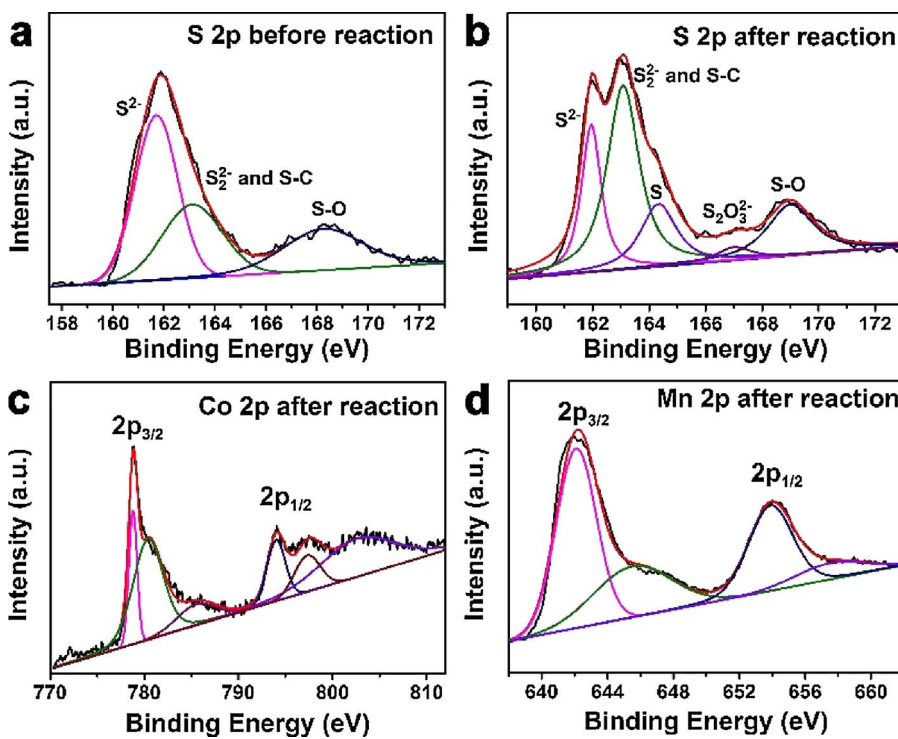


Fig. 7. High-resolution XPS spectra of S 2p (a) before and (b) after photocatalytic reaction, high-resolution XPS spectra of Co 2p (c) and Mn 2p (d) after photocatalytic reaction.

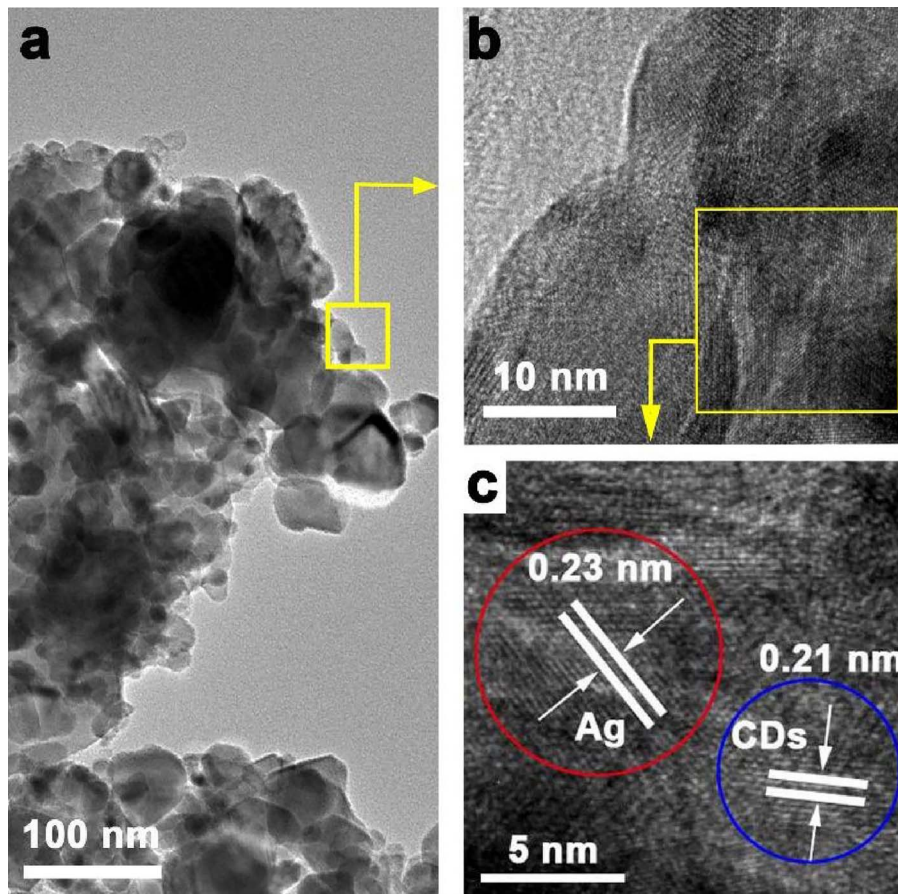


Fig. 8. TEM image (a) and HRTEM images (b and c) of CoMn-S/CDs with reduction sites. The red and blue circles represent Ag and CDs particles, respectively. (For interpretation of the references to colour in this figure legend, the reader is referred to the web version of this article.)

avoid recombination of photo induced electron-hole pairs and accept electrons to produce hydrogen. As illustrated in Fig. 9 (left part), MnS cannot produce hydrogen with the light wavelength above 413 nm and without the help of sacrificial agent. Fig. 9 (right part) shows CoMn-S/

CDs can easily absorb visible light ($420 \text{ nm} \leq \lambda \leq 700 \text{ nm}$) and generate photo-induced electron-hole pairs. Electrons will transfer from conduction band of CoMn-S to the surface of CDs to avoid recombination. CDs will serve as reduction sites and H^+ will be reduced to H_2 .

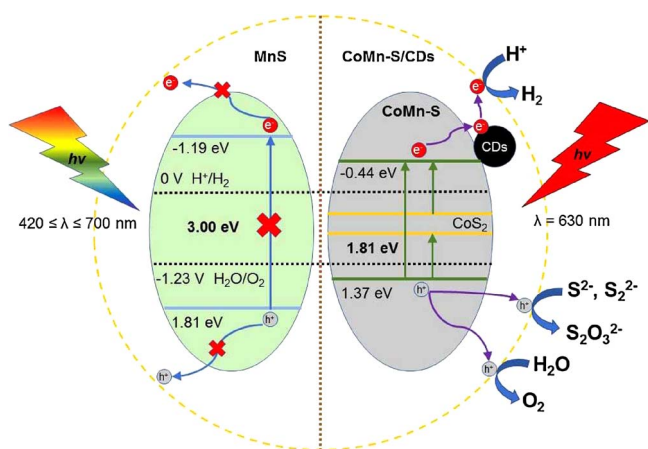


Fig. 9. The schematic illustration of band energy levels and charge transfers for the CoMn-S/CDs photocatalyst.

Parts of holes in the valence band of CoMn-S will go through the water oxidation pathway and oxidize H_2O to O_2 , while other holes will react with S^{2-} to form high oxidation state of S (such as $\text{S}_2\text{O}_3^{2-}$), causing photo-corrosion, which can be seen from high-resolution XPS spectrum of S 2p after photocatalytic reaction. It is of great importance that incorporation of CDs makes binary transition metal sulfide CoMn-S from no hydrogen-evolution to long wavelength visible-light-driven water splitting.

4. Conclusion

We demonstrate the design and fabrication of a new kind of photocatalyst CoMn-S/CDs by combining CDs and CoS_2 in MnS. The CoMn-S/CDs as photocatalyst could achieve from no hydrogen-evolution to long wavelength visible-light-driven water splitting. By controlling the amount of CDs, when the concentration of CDs is 0.039 g_{CDs}/g_{catalyst}, the CoMn-S/CDs exhibits excellent water splitting property with H_2 evolution rate of 0.421 $\mu\text{mol}/\text{h}$ and O_2 evolution rate of about 0.051 $\mu\text{mol}/\text{h}$ ($420 \text{ nm} \leq \lambda \leq 700 \text{ nm}$) while both MnS and CoMn-S have no hydrogen evolution ability. In particular, the H_2 evolution rate is 0.076 $\mu\text{mol}/\text{h}$ and O_2 evolution rate is about 0.010 $\mu\text{mol}/\text{h}$ when $\lambda = 535 \text{ nm}$ while the H_2 evolution rate is 0.024 $\mu\text{mol}/\text{h}$ and O_2 evolution rate is about 0.004 $\mu\text{mol}/\text{h}$ when $\lambda = 630 \text{ nm}$. It is also notable that CoMn-S/CDs exhibits well stability for about 4-time repetitive experiments, which is better than many other transition metal sulfides catalysts. The efficient photocatalytic ability may attribute to the synergistic effect of nanocomposite, in which MnS is the major component for photocatalysis, addition of CoS_2 enables the photocatalyst to capture light of wider range and CDs serve as reduction sites, which can accelerate the electron transfer to avoid recombination of photo induced electron-hole pairs and simultaneously accept electrons to produce hydrogen. This is the first example of an active long wavelength visible-light-driven photocatalyst consisting mainly of MnS.

Acknowledgements

This work is supported by the Collaborative Innovation Center of Suzhou Nano Science and Technology, the National Natural Science Foundation of China (51725204, 21771132, 51572179, 21471106, 51422207, 21501126), the Natural Science Foundation of Jiangsu Province (BK20161216) and a project funded by the Priority Academic Program Development of Jiangsu Higher Education Institutions (PAPD).

Appendix A. Supplementary data

Supplementary data associated with this article can be found, in the online version, at <https://doi.org/10.1016/j.apcatb.2017.12.047>.

References

- [1] A. Fujishima, K. Honda, *Nature* 238 (1972) 37–38.
- [2] H. Vrubel, D. Merki, X.L. Hu, *Energy Environ. Sci.* 5 (2012) 6136–6144.
- [3] Y.H. Chang, R.D. Nikam, C.T. Lin, J.K. Huang, C.C. Tseng, C.L. Hsu, C.C. Cheng, C.Y. Su, L.J. Li, D.H.C. Chua, *ACS Appl. Mater. Interfaces* 6 (2014) 17679–17685.
- [4] A. Kudo, Y. Miseki, *Chem. Soc. Rev.* 38 (2009) 253.
- [5] M.G. Walter, E.L. Warren, J.R. McKone, S.W. Boettcher, Q. Mi, E.A. Santori, N.S. Lewis, *Chem. Rev.* 110 (2010) 6446.
- [6] S.H. Wei, A. Zunger, *Phys. Rev. B* 48 (1993) 6111–6115.
- [7] X.V. Zhang, S.T. Martin, C.M. Friend, M.A.A. Schoonen, H.D. Holland, *J. Am. Chem. Soc.* 126 (2004) 11247–11253.
- [8] K. Ikeue, S. Shiiba, M. Machida, *ChemSusChem* 4 (2011) 269–273.
- [9] Q.C. Yuan, D. Liu, N. Zhang, W. Ye, H.X. Ju, L. Shi, R. Long, J.F. Zhu, Y.J. Xiong, *Angew. Chem. Int. Ed.* 56 (2017) 4206–4210.
- [10] L. Zhu, S.B. Jo, S. Ye, K. Ullah, Z.D. Meng, W.C. Oh, *J. Ind. Eng. Chem.* 22 (2015) 264–271.
- [11] J. Wang, B. Li, J.Z. Chen, N. Li, J.F. Zheng, J.H. Zhao, Z.P. Zhu, *Appl. Surf. Sci.* 259 (2012) 118–123.
- [12] B.L. Abrams, J.P. Wilcoxon, *Crit. Rev. Solid State Mater. Sci.* 30 (2005) 153–182.
- [13] H.T. Li, Z.H. Kang, Y. Liu, S.T. Lee, *J. Mater. Chem.* 22 (2012) 24230–24253.
- [14] H.J. Yu, R. Shi, Y.F. Zhao, G.I.N. Waterhouse, L.Z. Wu, C.H. Tong, T.R. Zhang, *Adv. Mater.* 28 (2016) 9454–9477.
- [15] X.Q. Wu, J. Zhao, S.J. Guo, L.P. Wang, W.L. Shi, H. Huang, Y. Liu, Z.H. Kang, *Nanoscale* 8 (2016) 17314–17321.
- [16] J. Liu, Y. Liu, N.Y. Liu, Y.Z. Han, X. Zhang, H. Huang, Y. Lifshitz, S.T. Lee, J. Zhong, Z.H. Kang, *Science* 347 (2015) 970–974.
- [17] X.Q. Wu, C. Zhu, L.P. Wang, S.J. Guo, Y.L. Zhang, H. Li, H. Huang, Y. Liu, J.W. Tang, Z.H. Kang, *ACS Catal.* 7 (2017) 1637–1645.
- [18] S.W. Yang, J. Sun, X.B. Li, W. Zhou, Z.Y. Wang, P. He, G.Q. Ding, X.M. Xie, Z.H. Kang, M.H. Jiang, *J. Mater. Chem. A* 2 (2014) 8660–8667.
- [19] Q. Li, Z.C. Xing, D.W. Wang, X.P. Sun, X.R. Yang, *ACS Catal.* 6 (2016) 2797–2801.
- [20] F. Fu, Y.F. Chen, P.J. Li, J.R. He, Z.G. Wang, W. Lin, W.L. Zhang, *RSC Adv.* 5 (2015) 71790–71795.
- [21] H.T. Li, R.H. Liu, W.Q. Kong, J. Liu, Y. Liu, L. Zhou, X. Zhang, S.T. Lee, Z.H. Kang, *Nanoscale* 6 (2014) 867–873.
- [22] L. Zhu, S.B. Jo, S. Ye, K. Ullah, Z.D. Meng, W.C. Oh, *J. Ind. Eng. Chem.* 22 (2015) 264–271.
- [23] R.L. Liu, D.Q. Wu, S.H. Liu, K. Koynov, W. Knoll, Q. Li, *Angew. Chem. Int. Ed.* 121 (2009) 4519–4743.
- [24] Y. He, L. Zhang, B. Teng, M. Fan, *Environ. Sci. Technol.* 49 (2015) 649–656.
- [25] Z.Z. Wu, X.Z. Yuan, H. Wang, Z.B. Wu, L.B. Jiang, H. Wang, L. Zhang, Z.H. Xiao, X.H. Chen, G.M. Zeng, *Appl. Catal. B Environ.* 202 (2017) 104–111.
- [26] Y. Yang, Q. Sun, Y.S. Li, H. Li, Z.W. Fu, *J. Power Sources* 223 (2013) 312–318.
- [27] C.b. Ouyang, X. Wang, S.Y. Wang, *Chem. Commun.* 51 (2015) 14160.
- [28] C. An, K. Tang, X. Liu, F. Li, G. Zhou, Y.J. Qian, *J. Cryst. Growth* 252 (2003) 575–580.
- [29] J. Li, S. Xiong, X. Li, Y. Qian, *Nanoscale* 5 (2013) 2045–2054.
- [30] Y.F. Tang, S.J. Chen, T. Chen, W.F. Guo, Y.S. Li, S.C. Mu, S.X. Yu, Y.F. Zhao, F.S. Wen, F.M. Gao, *J. Mater. Chem. A* 5 (2017) 3923.
- [31] G.H. Yue, P.X. Yan, J.Z. Liu, X.Y. Fan, R.F. Zhuo, *Appl. Phys. Lett.* 87 (2005) 262–505.
- [32] D. Sun, R. Ban, P.H. Zhang, G.H. Wu, J.R. Zhang, J.J. Zhu, *Carbon* 64 (2013) 424–434.
- [33] H. Ming, Z. Ma, Y. Liu, K.M. Pan, H. Yu, F. Wang, Z.H. Kang, *Dalton Trans.* 41 (2012) 9526–9531.
- [34] J. Liu, S.Y. Zhao, C.X. Li, M.M. Yang, Y.M. Yang, Y. Liu, Y. Lifshitz, S.T. Lee, Z.H. Kang, *Adv. Energy Mater.* 6 (2016) 1502039.
- [35] J. Zhang, J.G. Yu, Y.M. Zhang, Q. Li, J.R. Gong, *Nano Lett.* 11 (2011) 4774–4779.
- [36] S. Kervan, N. Kervan, *Intermetallics* 46 (2014) 45–50.
- [37] E. Kucur, J. Riegler, G.A. Urban, T. Nann, *J. Chem. Phys.* 119 (2003) 2333.
- [38] L. Bai, S. Qiao, Y. Fang, J.G. Tian, J. Mcleod, Y.L. Song, H. Huang, Y. Liu, Z.H. Kang, *J. Mater. Chem. C* 4 (2016) 8490–8495.
- [39] J. Pommerehne, H. Vestweber, W. Guss, R.F. Mahrt, H. Bässler, M. Porsch, J. Daub, *Adv. Mater.* 7 (1995) 551–554.
- [40] D. Patra, C.C. Chiang, W.A. Chen, K.H. Wei, M.C. Wu, C.W. Chu, *J. Mater. Chem. A* 1 (2013) 7767–7774.
- [41] H.W. Huang, R.R. Cao, S.X. Yu, K. Xu, W.C. Hao, Y.G. Wang, F. Dong, T.R. Zhang, Y.H. Zhang, *Appl. Catal. B Environ.* 219 (2017) 526–537.
- [42] H.W. Huang, S.C. Tu, C. Zeng, T.R. Zhang, A.H. Reshak, Y.H. Zhang, *Angew. Chem. Int. Ed.* 56 (2017) 11860–11864.
- [43] H.C. Zhang, H. Huang, H. Ming, H.T. Li, L.L. Zhang, Y. Liu, Z.H. Kang, *J. Mater. Chem.* 22 (2012) 10501.
- [44] V. Toniazza, C. Mustina, J.M. Portala, B. Humbert, R. Benoit, R. Errec, *Appl. Surf. Sci.* 143 (1999) 229–237.
- [45] H. Sekiyama, N. Kosugi, H. Kuroda, T. Ohta, *Bull. Chem. Soc. Jpn.* 59 (1986) 575.